Thermal conductivity of CaF_2 at high pressure

Somayeh Faraji,[1,2] S. Mehdi Vaez Allaei,[2] and Maximilian Amsler[3,4,*]
[1]*Department of Physics, Institute for Advanced Studies in Basic Sciences, P.O. Box 45195-1159, Zanjan, Iran*
[2]*Department of Physics, University of Tehran, P.O. Box 14395/547, Tehran, Iran*
[3]*Department of Chemistry and Biochemistry, University of Bern, Freiestrasse 3, CH-3012 Bern, Switzerland*
[4]*Department of Materials Science and Engineering, Cornell University, Ithaca, New York 14853, USA*

(Received 12 January 2021; revised 7 February 2021; accepted 16 March 2021; published 1 April 2021; corrected 6 April 2021)

We study the thermal transport properties of three CaF_2 polymorphs up to a pressure of 30 GPa using first-principles calculations and an interatomic potential based on machine learning. The lattice thermal conductivity κ is computed by iteratively solving the linearized Boltzmann transport equation and by taking into account three-phonon scattering. Overall, κ increases nearly linearly with pressure, and we show that the recently discovered δ-phase with $P\bar{6}2m$ symmetry and the previously known γ-CaF_2 high-pressure phase have significantly lower lattice thermal conductivities than the ambient-thermodynamic cubic fluorite ($Fm\bar{3}m$) structure. We argue that the lower κ of these two high-pressure phases stems mainly due to a lower contribution of acoustic modes to κ as a result of their small group velocities. We further show that the phonon mean free paths are very short for the $P\bar{6}2m$ and *Pnma* structures at high temperatures, and we use the Cahill-Pohl model to assess the lower limit of thermal conductivity in these domains.

DOI: 10.1103/PhysRevB.103.134301

I. INTRODUCTION

Calcium fluoride (CaF_2) has a variety of technological applications due to its remarkable optical properties and its high thermal stability [1–4]. At ambient conditions, α-CaF_2 crystallizes in the cubic fluorite structure with $Fm\bar{3}m$ symmetry. In this structure, CaF_2 exhibits a superwide band gap of 12 eV with excellent light transmission over a wide spectrum, and a high laser damage threshold. These properties render CaF_2 an ideal candidate for optical windows, main lens substrates in large-scale semiconductor microlithography systems, and photodetectors [1,4–8].

Cubic CaF_2 undergoes a sequence of structural phase transitions at increased pressures [9–17]. Above 8–10 GPa, CaF_2 transforms to the denser orthorhombic cotunnite γ-phase with *Pnma* symmetry, accompanied by an increased coordination number of Ca from 8 to 9. X-ray diffraction and Raman spectroscopy have shown that this high-pressure phase is stable up to 49 GPa at room temperature [11,12]. As pressure increases further, the stability of γ-CaF_2 decreases, and above 72 GPa a further transition occurs to a hexagonal $P6_3/mmc$ phase [17].

In addition to these experimentally observed low-temperature high-pressure phases, high-temperature modifications thereof have been studied predominantly using computational models. Using *ab initio* structural searches, Nelson *et al.* recently proposed a hypothetical structure with $P\bar{6}2m$ symmetry as a high-temperature polymorph of γ-CaF_2, referred to as δ-CaF_2 [18]. Similar to its ambient-pressure counterpart, δ-CaF_2 is predicted to undergo a transition to a superionic phase with bcc structure at temperatures exceeding ≈2500 K at 20 GPa [19].

Despite these theoretical studies, little is known about the high-pressure behavior of the thermal transport properties in CaF_2 polymorphs. At ambient pressure, the lattice thermal conductivity of α-CaF_2 has been studied both through experiments and computations. In two separate early experiments in 1957 and 1960, the near room-temperature value of the lattice thermal conductivity was measured to be 5.5 [20] and 9.5 [21] $\mathrm{W\,m^{-1}\,K^{-1}}$, respectively. Later, Slack [22] reported a value of 11.69 $\mathrm{W\,m^{-1}\,K^{-1}}$ in 1961. Theoretical room-temperature values from simulations have been predicted in the range of 7.0–8.6 $\mathrm{W\,m^{-1}\,K^{-1}}$ [23,24]. To the best of our knowledge, the only work on the pressure dependence of κ in α-CaF_2 reported $9.7 < \kappa < 10.9$ $\mathrm{W\,m^{-1}\,K^{-1}}$, measured using a dynamic two-strip method at room temperature in a narrow pressure range of 0.1–1.0 GPa [25].

In this work, we study the thermal conductivity of the α, γ, and δ phases of CaF_2 as a function of pressure in the range of 0–30 GPa. To alleviate the computational burden of *ab initio* calculations, we resort to using an efficient machine-learning interatomic potential, as trained in our previous work [26], to accelerate the assessment of the lattice thermal conductivity κ. We show that the value of κ for the γ-CaF_2 and δ-CaF_2 phases is lower than that of the α phase across the whole pressure domain. In particular, the extremely small phonon mean free paths in these two phases lead to a potential breakdown of the Boltzmann transport equation (BTE). Hence, we assess the validity of the BTE results based on the amorphous limit using the Cahill-Pohl model, and we draw the associated temperature-pressure transition boundary.

II. METHODS

A. Interatomic potential

We use CENT, a neural-network-based interatomic potential, that takes into account charge transfers to model the ionic

---

[*] Corresponding author: amsler.max@gmail.com

bonding in CaF_2 [27]. The construction of the CaF_2 CENT potential is discussed in detail elsewhere [26], and we employ its implementation in the FLAME package [28–30]. The particular parametrization of our CENT potential has been used elsewhere to obtain the physical properties of CaF_2 [26] and to study the surface morphologies of CaF_2 [31].

B. Density functional theory

Structural relaxations and single-point total energy calculations were performed with density functional theory (DFT) calculations at selected pressures of 2, 10, and 30 GPa. We used the plane-wave QUANTUM ESPRESSO simulation package [32,33] in conjunction with the Perdew-Burke-Ernzerhof (PBE) [34] parametrization of the exchange-correlation functional and ultrasoft pseudopotentials [35]. The wave functions and electron densities were expanded with a plane-wave basis set up to a kinetic cutoff energy of 45 and 540 Ry, respectively. The Brillouin zone was sampled using $16 \times 16 \times 16$, $14 \times 14 \times 16$, and $14 \times 16 \times 14$ Monkhorst-Pack [36] k-points meshes for α-CaF_2, δ-CaF_2, and γ-CaF_2, respectively. The atomic positions were relaxed until the maximal force acting on the atoms was less than 1×10^{-5} Ry/Bohr.

C. Phonons

The second-order interatomic force constants were calculated with the finite-difference approach using the supercell method as implemented in the PHONOPY package [37]. The atomic forces were either computed with DFT or CENT. Supercells of dimension $4 \times 4 \times 4$, $2 \times 3 \times 2$, and $2 \times 2 \times 4$ were used for α-CaF_2, γ-CaF_2, and δ-CaF_2, respectively, leading to cells consisting of 192, 144, and 144 atoms. A finite-difference step size of 0.01 Å was applied to displace the atoms. A **q**-point mesh of $50 \times 50 \times 50$ was used for the BZ integration.

D. BTE thermal transport

The thermal transport calculations were carried out by taking into account anharmonic three-phonon interactions. Third-order force constants were computed from finite differences using the supercell method with the same sizes used in the calculations of the second-order force constants. Atomic displacements were created using the `thirdorder.py` script included in the SHENGBTE distribution [38], taking into account up to the fifth-nearest neighbors to truncate the three-body interactions, which gives well-converged values of κ. The atomic forces were either computed with DFT or CENT. The thermal conductivity in the BTE is given by [39]

$$\kappa = \frac{1}{3VN_q} \sum_{q\gamma} C_{q\gamma} \mathbf{v}_{q\gamma}^2 \tau_{q\gamma}, \tag{1}$$

where V is the volume of the cell containing N atoms, q refers to the wave vector in the first Brillouin zone, N_q is the number of discrete q-points, γ is the mode index that refers to different phonon branches, $C_{q\gamma}$ denotes the mode specific heat capacity at constant volume, $\mathbf{v}$ is the phonon group velocity ($\mathbf{v}_{q\gamma} = \nabla_q \omega_{q\gamma}$), and τ is the phonon lifetime, which is related to the phonon mean free path (MFP) $\lambda = \mathbf{v} \cdot \tau$.

The detailed effects of the cutoff-distance on the thermal conductivities are shown in Sec. S3 of the Supplemental Material (SM) [42]. The second- and third-order interatomic force constants were fed into the SHENGBTE package to calculate κ by iteratively solving the linearized phonon Boltzmann transport equation for temperatures ranging from 100 to 900 K. Both isotropic and three-phonon scattering were considered. The isotropic scattering rates were calculated by applying the Pearson deviation coefficients incorporated in SHENGBTE. The so-called proportionality constant *scalebroad*, related to the adaptive Gaussian broadening technique, was set to 0.2 in all the SHENGBTE calculations, together with $19 \times 19 \times 19$, $19 \times 19 \times 19$, and $15 \times 15 \times 12$ **q**-point grids for α-CaF_2, δ-CaF_2, and γ-CaF_2, respectively.

E. Cahill-Pohl model

We estimate the amorphous limit of the thermal conductivity κ_{CP} using the Cahill-Pohl model [40], which is an extension of the Einstein model. While Einstein assumed that the thermal energy is transported between neighboring atoms vibrating with a single frequency, the Cahill-Pohl model proposes that the energy is transferred between collective vibrations. Therefore, the model includes a range of frequencies, instead of a single frequency used by Einstein. In this model, the thermal conductivity is expressed as follows (details can be found in Ref. [41]):

$$\kappa_{CP} = \left(\frac{\pi}{6}\right)^{\frac{1}{3}} k_B n^{\frac{2}{3}} \sum_\alpha v_\alpha \left(\frac{T}{T_\alpha^D}\right)^2 \int_0^{T_\alpha^D/T} \frac{x^3 e^x}{(e^x - 1)^2} dx,$$
$$x = \frac{T_\alpha^D}{T}, \tag{2}$$

where n is the density of the atoms in the solid (m^{-3}), and v_α is the low-frequency speed of sound (from acoustic phonons) for polarization α. $T_\alpha^D = \frac{\hbar}{k_B} v_\alpha (6n\pi^2)^{\frac{1}{3}}$ is the characteristic temperature equivalent to the Debye temperature for that polarization, which corresponds to the activation of all phonons. x is the reduced phonon energy, and the summation runs over the vibrational polarizations (one longitudinal and two transverse acoustic branches). The v_α of each acoustic group velocity was determined using harmonic lattice dynamics from Sec. II C.

III. RESULTS AND DISCUSSION

We start out by validating the quality and predictive power of our CENT potential with respect to DFT results based on the three relevant phases α-CaF_2, γ-CaF_2, and δ-CaF_2. The thermodynamic properties including the transition pressures are well reproduced by CENT. As shown in Fig. S1 of the SM [42], the phase transition from α-CaF_2 to γ-CaF_2 occurs at 8 GPa, which is close to the experimental measurements. Also, the enthalpy differences of the δ-CaF_2 and γ-CaF_2 decrease with increasing pressure. In fact, these two high-pressure phases are energetically very close to each other, i.e., dropping from 12.7 to 2.1 meV/at in the pressure range between 2 and 30 GPa. We then compare the dynamical properties predicted by the CENT potential with DFT values at 2 GPa. The phonons arising from the CENT potential as well

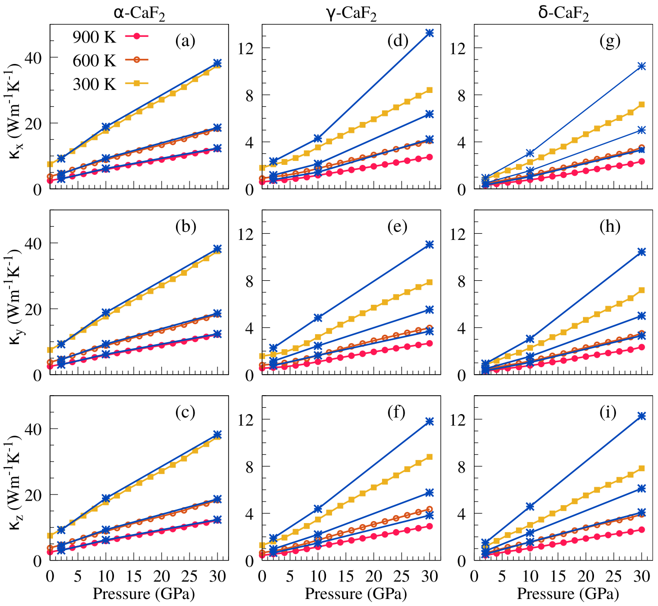

FIG. 1. The components of the lattice thermal conductivities $\kappa_{x,y,z}$ of α-$\mathrm{CaF_2}$ [panels (a)–(c)], γ-$\mathrm{CaF_2}$ [panels (d)–(f)], and δ-$\mathrm{CaF_2}$ [panels (g)–(i)] as a function of pressure at temperatures of 300, 600, and 900 K. DFT data are shown with blue crosses, while CENT results are shown with yellow squares (300 K), orange circles (600 K), and pink dots (900 K).

as the phonon DOS agree well with the results from DFT (see Fig. S2 in the SM [42]). Similarly, the lattice thermal conductivities from CENT are in excellent agreement with the DFT predictions, as shown in Fig. S3 in the SM [42].

Next, we study the evolution of the thermal conductivity of the three phases as a function of pressure. Since the δ-$\mathrm{CaF_2}$ phase exhibits imaginary phonon modes at 0 GPa, we focus on the pressure regime between 2 and 30 GPa within which all structures are dynamically stable. Figure 1 plots the components $\kappa_{x,y,z}$ of the thermal conductivity at selected temperatures, and it shows that their values increase almost linearly with pressure. This increase in thermal conductivity can be rationalized in a first approximation by the decrease in volume V in the denominator in Eq. (1) as the pressure increases. The room-temperature thermal conductivity of all three phases at different pressures and room temperature is also summarized in Table I

In Fig. 1 we also include the values of $\kappa_{x,y,z}$ at selected pressures from DFT calculations. While the relative error between CENT and DFT for the α-phase is small at all pressures, the discrepancy increases with pressure for γ-$\mathrm{CaF_2}$ and δ-$\mathrm{CaF_2}$. Nevertheless, the qualitative trend is well captured, and the *absolute* error remains small (note that the scale of the y-axis differs between the different phases in Fig. 1). In Fig. S5 of the SM [42] we show the evolution of the ratio $\kappa_{x,y,z}(T)/\kappa_{x,y,z}(300\ \mathrm{K})$ as a function of pressure for the various phases and at various temperatures T. The agreement between CENT and DFT is excellent, indicating that the change in phonon scattering rates as a function of pressure is correctly captured by our machine-learning potential. Further, note that the CENT potential was trained exclusively on cluster structures where the training data were only based on the energies, in contrast to other machine-learning approaches that explicitly train on atomic forces [43,44]. Given that the CENT model was trained without seeing a single high-pressure structure, it performs surprisingly well, correctly capturing the general behavior of the system.

At all pressures, α-$\mathrm{CaF_2}$ has a significantly higher value of κ than either of the other two phases at a given temperature. Table I also contains the room-temperature zero-pressure value of the thermal conductivity, $\kappa_{\mathrm{ambient}}$, of α-$\mathrm{CaF_2}$ from other theoretical studies in the literature. We obtain $\kappa_{\mathrm{ambient}} = 7.5\ \mathrm{W\,m^{-1}\,K^{-1}}$, which is close to the value of $7.0\ \mathrm{W\,m^{-1}\,K^{-1}}$ reported by Plata *et al.* [45]. In comparison with experimental results from Andersson *et al.*, our value of $\kappa_{\mathrm{ambient}}$ is about 2.2 $\mathrm{W\,m^{-1}\,K^{-1}}$ lower than the experimental measurement of 9.7 $\mathrm{W\,m^{-1}\,K^{-1}}$ through a two-strip method [25].

Our values of κ for δ-$\mathrm{CaF_2}$ and γ-$\mathrm{CaF_2}$ show that, unlike α-$\mathrm{CaF_2}$, these two phases exhibit slight anisotropies along their three components. At 300 K, the components of $\kappa_{x,y,z}$ for the γ-$\mathrm{CaF_2}$ and δ-$\mathrm{CaF_2}$ phases at 2 GPa are approximately $\{2.1, 1.7, 1.6\}$ and $\{0.8, 0.8, 1.2\}$ $\mathrm{W\,m^{-1}\,K^{-1}}$, respectively, while κ itself is 1.8 and 0.93 $\mathrm{W\,m^{-1}\,K^{-1}}$ for γ-$\mathrm{CaF_2}$ and δ-$\mathrm{CaF_2}$, respectively. The very low thermal conductivity of the δ-phase at low pressures can be primarily attributed to the soft acoustic phonon mode along K-Γ in the first Brillouin zone. (see Sec. S4 and Fig. S6 in the SM [42]).

There are several factors leading to the deceased κ of γ-$\mathrm{CaF_2}$ and δ-$\mathrm{CaF_2}$ compared to the cubic structure. Equation (1) contains the product of heat capacity, phonon group velocity, and phonon mean free path, the effects of which we can study individually. We first investigate the heat capacity per unit volume at selected pressure and temperatures, and we

TABLE I. The components of the lattice thermal conductivity $\kappa_{x,y,z}$ using CENT in units of $\mathrm{W\,m^{-1}\,K^{-1}}$ at 300 K and at selected pressures, together with available values from the literature. Results from DFT calculations are given in parantheses.

Phase	Components of κ	0 GPa	2 GPa	10 GPa	20 GPa	30 GPa
α-$\mathrm{CaF_2}$	$\kappa_x = \kappa_y = \kappa_z$	7.5	9.4 (9.2)	17.6 (18.8)	27.1	37.5 (38.2)
		7.04 [45], 8.6 [24], 7.0 ±0.39 [23]				
δ-$\mathrm{CaF_2}$	$\kappa_x = \kappa_y$		0.9 (0.9)	2.3 (2.9)	4.6	7.2 (10.0)
	κ_z		1.2 (1.5)	3.0 (4.5)	5.5	7.8 (12.4)
	κ_x	1.8	2.1 (2.3)	3.5 (4.1)	5.9	8.4 (12.3)
γ-$\mathrm{CaF_2}$	κ_y	1.6	1.7 (2.3)	3.2 (4.8)	5.7	7.9 (10.8)
	κ_z	1.3	1.6 (1.9)	3.5 (4.6)	6.2	8.8 (12.5)

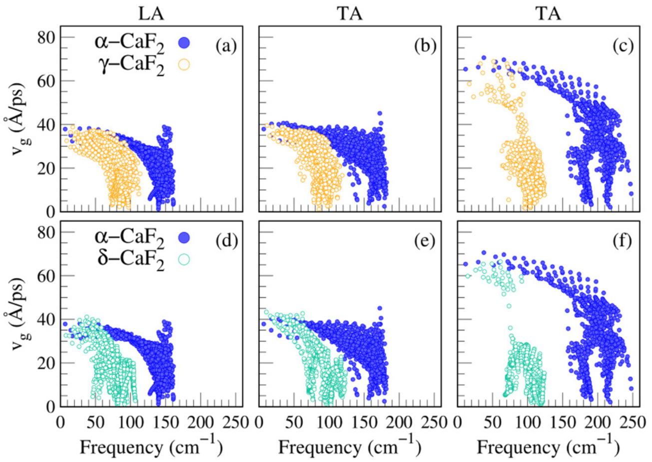

FIG. 2. Group velocities of the longitudinal and transversal acoustic modes as functions of frequency for γ-CaF$_2$ [(a)–(c)] and δ-CaF$_2$ [(d)–(f)] in comparison with α-CaF$_2$ at 300 K and 2 GPa.

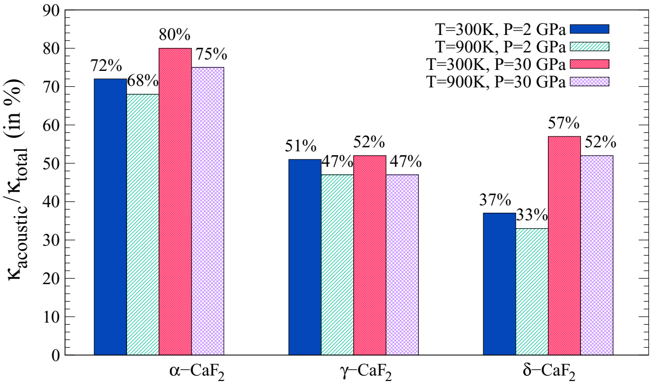

FIG. 3. The fraction of acoustic modes κ_{acoustic} contributing to the total thermal conductivity κ_{total} at pressures of 2 and 30 GPa and temperatures of 300 and 900 K for the three relevant CaF$_2$ phases.

show its evolution in Fig. S4 of the SM [42]. The heat capacity increases rapidly with temperature T, and it is proportional to T^3 at low T, whereas it tends to a constant value at a high temperature, following the Dulong-Petit law. In the case of α-CaF$_2$, the obtained value for C_v at zero pressure and at temperature 300 K is 65.57 Jm^{-1}K^{-1}, which is comparable with the experimental value of 67.11 Jm^{-1}K^{-1} [25]. The obtained values of C_v at temperature 300 K and pressure 2 GPa for α-CaF$_2$, δ-CaF$_2$, and γ-CaF$_2$ are 64.92, 65.10, and 64.64 Jm^{-1}K^{-1}, respectively. The value of C_v decreases with increasing pressure (see the insets in Fig. S4 of the SM [42]) at given temperature, and at 30 GPa it reaches 58.29, 59.77, and 59.54 Jm^{-1}K^{-1} for α-CaF$_2$, δ-CaF$_2$, and γ-CaF$_2$, respectively. Overall, the difference in C_v among the three phases is minute (within less than 3%) and cannot account for the strong deviations of κ.

We now turn our attention to the group velocities v_g of the acoustic phonon modes, which are in general responsible for a large fraction of the thermal transport. Figure 2 shows v_g of the longitudinal and transverse acoustic (LA and TA) branches of γ-CaF$_2$ and δ-CaF$_2$, plotted on top of the values of α-CaF$_2$. Note that the δ-phase exhibits a particularly soft acoustic branch with a low v_g along K-Γ (see Fig. S6 in the SM [42]). Overall, α-CaF$_2$ has larger group velocities than either γ-CaF$_2$ or δ-CaF$_2$. To quantify the difference in the group velocities, we consider the mean values of the LA and the two TA modes, $\bar{v}_g^{\text{LA}}$, $\bar{v}_g^{\text{TA}_1}$, and $\bar{v}_g^{\text{TA}_2}$. The ratios of these average velocities of α-CaF$_2$ with respect to the γ- and δ-phases are $\{\bar{v}_g^{\text{LA}}, \bar{v}_g^{\text{TA}_1}, \bar{v}_g^{\text{TA}_2}\}_\alpha/\{\bar{v}_g^{\text{LA}}, \bar{v}_g^{\text{TA}_1}, \bar{v}_g^{\text{TA}_2}\}_\gamma = \{1.7, 1.7, 1.9\}$ and $\{\bar{v}_g^{\text{LA}}, \bar{v}_g^{\text{TA}_1}, \bar{v}_g^{\text{TA}_2}\}_\alpha/\{\bar{v}_g^{\text{LA}}, \bar{v}_g^{\text{TA}_1}, \bar{v}_g^{\text{TA}_2}\}_\delta = \{1.7, 1.6, 1.93\}$. Hence, the group velocities of α-CaF$_2$ are almost twice as high as the corresponding values in γ-CaF$_2$ and δ-CaF$_2$.

Further, the contributions of acoustic modes to the thermal transport are influenced by their interaction with the optical modes, i.e., the amount of heat that is scattered through optical phonons. In general, phases with larger, complex structures tend to have larger contributions from optical scattering, with stronger coupling between acoustic and optical modes. Figure 3 shows the fraction of acoustic modes contributing to the total thermal conductivity, $r_\kappa = \kappa_{\text{acoustic}}/\kappa_{\text{total}}$ for the α, γ, and δ phase. At any pressure and temperature, α-CaF$_2$ exhibits the largest value of r_κ. Both γ-CaF$_2$ and δ-CaF$_2$ show strong contributions of optical phonon scattering, in particular for δ-CaF$_2$ at low lower pressures. Again, this behavior can be attributed to the soft-mode in one of the acoustic branches of δ-CaF$_2$ at 2 GPa, which becomes less pronounced with increasing pressure, as shown in Fig. S6 in the SM [42].

We also compare the phonon MFP in Fig. 4 at 2 and 30 GPa at a temperature of 300 K. Overall, the MFPs of the α-phase are longer than either of the high-pressure phases. In fact, the MFPs of a significant fraction of modes are shorter than the average interatomic distance of ≈2.4 Å in both the γ- and δ-phases, leading to an inaccurate description of thermal transport within the BTE by dramatically underestimating the value of κ [46].

To address this issue, we assess the limitations of the BTE by comparing its results to the Cahill-Pohl model, which provides an estimate of the lower bound in the amorphous limit,

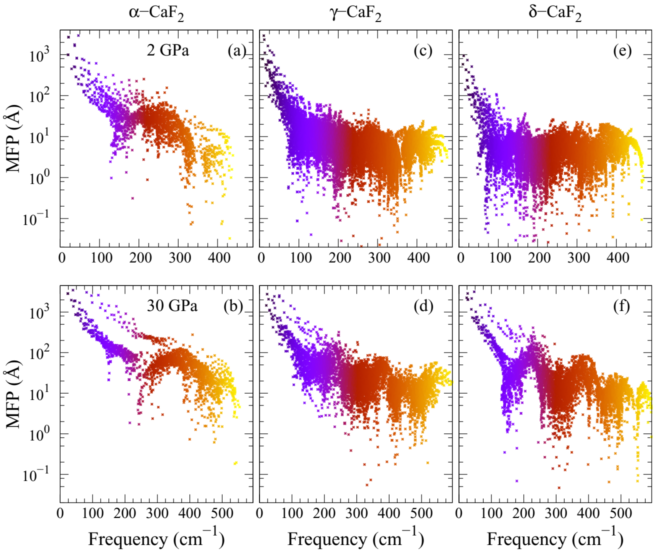

FIG. 4. Phonon mean free path (MFP) of all phonon modes as a function of frequency at pressures of 2 GPa (first row) and 30 GPa (second row) of α-CaF$_2$ [panels (a) and (b)], γ-CaF$_2$ [panels (c) and (d)], and δ-CaF$_2$ [panels (e) and (f)].

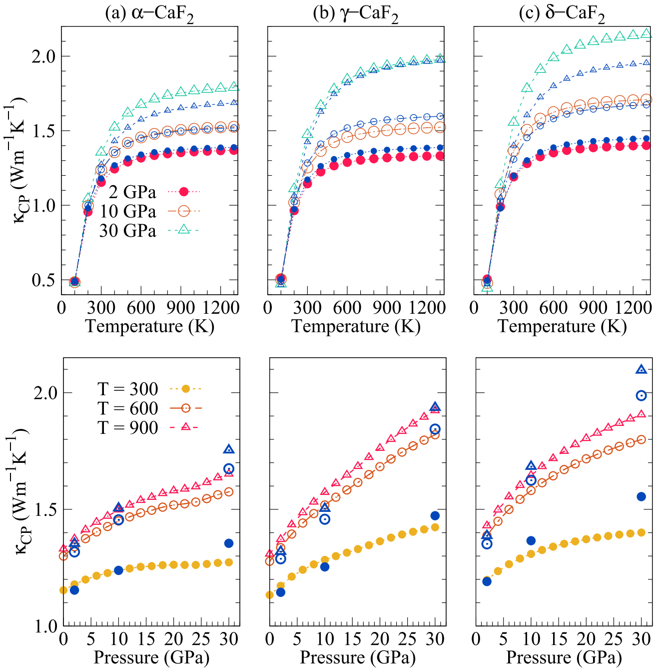

FIG. 5. The amorphous limit of the thermal conductivity κ_{CP} based on the Cahill-Pohl model of (a) α-CaF_2, (b) γ-CaF_2, and (c) δ-CaF_2 based on CENT calculations as a function of temperature at selected pressures (first row) and as a function of pressure for temperatures 300, 600, and 900 K (second row). DFT results at 2, 10, and 30 GPa are shown with blue symbols.

κ_{CP}. Figure 5 shows the values of κ_{CP} as a function of temperature and pressures for the α, γ, and δ-CaF_2. We observe two very clear trends: (a) κ_{CP} increases with temperature at a given pressure, plateauing out above ≈600 K (see the top row in Fig. 5), and (b) κ_{CP} increases steadily with pressure at constant temperature (see the bottom row in Fig. 5). The values of κ_{CP} are particularly high for δ-CaF_2, which indicates that an especially large error can be expected in the BTE model.

To assess the limits of the BTE, we map out the boundary in T and p where κ_{BTE} drops below the amorphous limit, κ_{CP}. Figure 6 plots κ_{BTE} and κ_{CP} at selected temperatures as a function of pressure. For α-CaF_2, the thermal conductivities predicted through the BTE are reliable, as their values remain above κ_{CP} for all pressures and temperatures considered here. However, the BTE breaks down for δ-CaF_2 and γ-CaF_2, especially at high temperatures and low pressures. The transition boundary where κ_{BTE} crosses κ_{CP} in T and p is mapped out in Fig. 6(g), showing that BTE only yields reliable results within the regime of high pressure and low temperatures.

IV. CONCLUSIONS

In summary, we studied the effects of pressure and temperature on the thermal transport properties of three crystalline CaF_2 phases, using DFT and a machine-learning-based interatomic potential, CENT. The CENT potential gives results in good agreement with DFT, despite being trained exclusively on the energetics of cluster structures. Our results show that the two high-pressure phases, δ-CaF_2 and γ-CaF_2, exhibit significantly lower thermal conductivities κ than the cubic α-phase. We argue that the source of this large difference in κ stems from lower group velocities of the acoustic modes, and the larger contributions of phonon scattering events involving the optical modes in the δ- and γ-phase, which additionally impedes the transport of heat. A careful analysis of the phonon scattering shows that the MFPs (and the associated phonon lifetimes) are extremely short for the δ- and γ-phases, leading to the low values of κ. In fact, for high temperatures and at low pressures the MFPs are so short that they drop below the mean atomic bond lengths, and we expect that the thermal conductivity will eventually converge to the amorphous limit, which we estimate using the Cahill-Pohl model. Despite these limitations, our results show that the high-pressure phases exhibit around a factor of 5 times lower thermal conductivity than the ambient ground state.

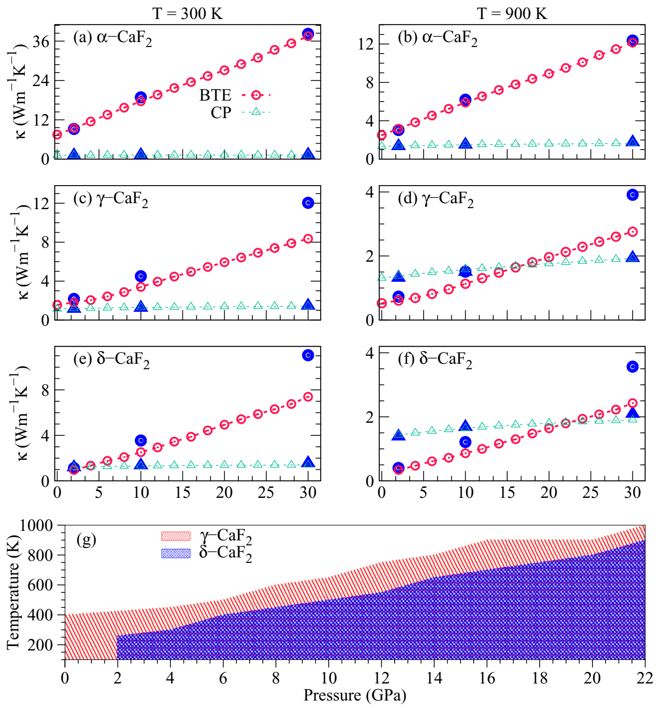

FIG. 6. The thermal conductivity κ as a function of pressure for α-CaF_2 [(a) and (b)], γ-CaF_2 [(c) and (d)], and δ-CaF_2 [(e) and (f)] with the Cahill-Pohl model (green triangles) at 300 and 900 K together with the results of BTE (red circles) at the same conditions. The values obtained from DFT results are shown with blue symbols. The calculated transition boundary where $\kappa_{\mathrm{CP}} > \kappa_{\mathrm{BTE}}$ for γ-CaF_2 and δ-CaF_2 is shown in panel (g), where the shaded regions indicate the T-p range of reliable BTE results.

Our results show that the CENT potential qualitatively reproduces the DFT thermal conductivity with high accuracy, while requiring fewer than four orders of magnitude in computer resources. Hence, CENT will be particularly useful for predicting materials properties that require large simulation cells that are intractable at the level of DFT. Modeling the thermal transport of the amorphous phase with nonequilibrium molecular dynamics, the estimation of the transition temperature and properties of the superionic phases, and studying the transformation kinetics of phase transitions between the various high-pressure and high-temperature phases of $\mathrm{CaF_2}$ are only a few of the potential applications of CENT, and they will be the focus of our future research.

ACKNOWLEDGMENT

We highly appreciate fruitful discussions with Alireza Ghasemi and his insightful comments and contributions to this work. M.A. acknowledges support from the Swiss National Science Foundation (project P4P4P2-180669). S.F. acknowledges support from the Iran Science Elites Federation. S.F. and S.M.V.A. acknowledge partial support by the Research Council of the University of Tehran. S.M.V.A. acknowledges support from Iran National Science Foundation (INSF) through Grant No. 98023445.

[1] W. Liang, V. Ilchenko, D. Eliyahu, A. Savchenkov, A. Matsko, D. Seidel, and L. Maleki, Nat. Commun. **6**, 7371 (2015).

[2] C. Cazorla and D. Errandonea, Phys. Rev. Lett. **113**, 235902 (2014).

[3] A. Lyberis, A. J. Stevenson, A. Suganuma, S. Ricaud, F. Druon, F. Herbst, D. Vivien, P. Gredin, and M. Mortier, Opt. Mater. (Amsterdam) **34**, 965 (2012).

[4] L. Sang, M. Liao, Y. Koide, and M. Sumiya, Appl. Phys. Lett. **98**, 3502 (2011).

[5] V. Liberman, T. Bloomstein, M. Rothschild, J. Sedlacek, R. Uttaro, A. Bates, C. Van Peski, and K. Orvek, J. Vac. Sci. Technol. B **17**, 3273 (1999).

[6] M. Daimon and A. Masumura, Appl. Opt. **41**, 5275 (2002).

[7] C. Wagner and N. Harned, Nat. Photon. **4**, 24 (2010).

[8] X. C. Luo, J. N. Sun, W. L. Chang, and J. M. Ritchie, Key Engineering Materials **516**, 408 (2012).

[9] K.-F. Seifert, Ber. Bunsenges. Phys. Chem. **70**, 1041 (1966).

[10] D. P. Dandekar and J. C. Jamieson, Trans. Am. Crystallogr. Assoc. **5**, 19 (1969).

[11] L. Gerward, J. S. Olsen, S. Steenstrup, M. Malinowski, S. Åsbrink, and A. Waskowska, J. Appl. Crystallogr. **25**, 578 (1992).

[12] S. Speziale and T. S. Duffy, Phys. Chem. Miner. **29**, 465 (2002).

[13] J. H. Burnett, Z. H. Levine, and E. L. Shirley, Phys. Rev. B **64**, 241102(R) (2001).

[14] X. Wu, S. Qin, and Z. Wu, Phys. Rev. B **73**, 134103 (2006).

[15] H. Shi, W. Luo, B. Johansson, and R. Ahujia, J. Phys.: Condens. Matter **21**, 415501 (2009).

[16] F. El'kin, O. Tsiok, L. Khvostantsev, and V. Brazhkin, J. Exp. Theor. Phys. **100**, 971 (2005).

[17] S. M. Dorfman, F. Jiang, Z. Mao, A. Kubo, Y. Meng, V. B. Prakapenka, and T. S. Duffy, Phys. Rev. B **81**, 174121 (2010).

[18] J. R. Nelson, R. J. Needs, and C. J. Pickard, Phys. Rev. B **95**, 054118 (2017).

[19] J. R. Nelson, R. J. Needs, and C. J. Pickard, Phys. Rev. B **98**, 224105 (2018).

[20] F. Charvat and W. Kingery, J. Am. Ceram. Soc. **40**, 306 (1957).

[21] K. A. McCarthy and S. S. Ballard, J. Appl. Phys. **31**, 1410 (1960).

[22] G. A. Slack, Phys. Rev. **122**, 1451 (1961).

[23] P. Lindan and M. Gillan, J. Phys.: Condens. Matter **3**, 3929 (1991).

[24] Y.-Y. Qi, T. Zhang, Y. Cheng, X.-R. Chen, D.-Q. Wei, and L.-C. Cai, J. Appl. Phys. **119**, 095103 (2016).

[25] S. Andersson and G. Backstrom, J. Phys. C **20**, 5951 (1987).

[26] S. Faraji, S. A. Ghasemi, S. Rostami, R. Rasoulkhani, B. Schaefer, S. Goedecker, and M. Amsler, Phys. Rev. B **95**, 104105 (2017).

[27] S. A. Ghasemi, A. Hofstetter, S. Saha, and S. Goedecker, Phys. Rev. B **92**, 045131 (2015).

[28] M. Amsler, S. Rostami, H. Tahmasbi, E. R. Khajehpasha, S. Faraji, R. Rasoulkhani, and S. A. Ghasemi, Comput. Phys. Commun. **256**, 107415 (2020).

[29] H. A. Eivari, S. A. Ghasemi, H. Tahmasbi, S. Rostami, S. Faraji, R. Rasoulkhani, S. Goedecker, and M. Amsler, Chem. Mater. **29**, 8594 (2017).

[30] R. Rasoulkhani, H. Tahmasbi, S. A. Ghasemi, S. Faraji, S. Rostami, and M. Amsler, Phys. Rev. B **96**, 064108 (2017).

[31] S. Faraji, S. A. Ghasemi, B. Parsaeifard, and S. Goedecker, Phys. Chem. Chem. Phys. **21**, 16270 (2019).

[32] P. Giannozzi, S. Baroni, N. Bonini, M. Calandra, R. Car, C. Cavazzoni, D. Ceresoli, G. L. Chiarotti, M. Cococcioni, I. Dabo, A. Dal Corso, S. de Gironcoli, S. Fabris, G. Fratesi, R. Gebauer, U. Gerstmann, C. Gougoussis, A. Kokalj, M. Lazzeri, L. Martin-Samos, N. Marzari, F. Mauri, R. Mazzarello, S. Paolini, A. Pasquarello, L. Paulatto, C. Sbraccia, S. Scandolo, G. Sclauzero, A. P. Seitsonen, A. Smogunov, P. Umari, and R. M. Wentzcovitch, J. Phys.: Condens. Matter **21**, 395502 (2009).

[33] P. Giannozzi, O. Andreussi, T. Brumme, O. Bunau, M. B. Nardelli, M. Calandra, R. Car, C. Cavazzoni, D. Ceresoli, M. Cococcioni, N. Colonna, I. Carnimeo, A. Dal Corso, S. de Gironcoli, P. Delugas, R. A. DiStasio Jr., A. Ferretti, A. Floris, G. Fratesi, G. Fugallo, R. Gebauer, U. Gerstmann, F. Giustino, T. Gorni, J. Jia, M. Kawamura, H.-Y. Ko, A. Kokalj, E. Küçükbenli, M. Lazzeri, M. Marsili, N. Marzari, F. Mauri, N. L. Nguyen, H.-V. Nguyen, A. Otero-de-la-Roza, L. Paulatto, S. Ponc, D. Rocca, R. Sabatini, B. Santra, M. Schlipf, A. P. Seitsonen, A. Smogunov, I. Timrov, T. Thonhauser, P. Umari, N. Vast, X. Wu, and S. Baroni, J. Phys.: Condens. Matter **29**, 465901 (2017).

[34] J. P. Perdew, K. Burke, and M. Ernzerhof, Phys. Rev. Lett. **77**, 3865 (1996).

[35] D. Vanderbilt, Phys. Rev. B **41**, 7892 (1990).

[36] H. J. Monkhorst and J. D. Pack, Phys. Rev. B **13**, 5188 (1976).

[37] A. Togo and I. Tanaka, Scr. Mater. **108**, 1 (2015).

[38] W. Li, J. Carrete, N. A. Katcho, and N. Mingo, Comput. Phys. Commun. **185**, 1747 (2014).

[39] T. Luo, J. Garg, J. Shiomi, K. Esfarjani, and G. Chen, Europhys. Lett. **101**, 16001 (2013).

[40] D. G. Cahill and R. O. Pohl, Annu. Rev. Phys. Chem. **39**, 93 (1988).

[41] M. Kaviany, *Heat Transfer Physics* (Cambridge University Press, Cambridge, 2014).

[42] See Supplemental Material at http://link.aps.org/supplemental/10.1103/PhysRevB.103.134301 for validation benchmarks of the CENT potential, and convergence tests with respect to thermodynamic stability, phonon dispersion, and thermal transport properties.
[43] E. Minamitani, M. Ogura, and S. Watanabe, Appl. Phys. Express **12**, 095001 (2019).
[44] R. Li, E. Lee, and T. Luo, Mater. Today Phys. **12**, 100181 (2020).
[45] J. J. Plata, P. Nath, D. Usanmaz, J. Carrete, C. Toher, M. de Jong, M. Asta, M. Fornari, M. B. Nardelli, and S. Curtarolo, npj Comput. Mater. **3**, 45 (2017).
[46] P. B. Allen and J. L. Feldman, Phys. Rev. B **48**, 12581 (1993).

Correction: The omission of support information and a statement of thanks in the Acknowledgment section has been remedied.